Carbon 149 (2019) 390–399

Contents lists available at ScienceDirect

Carbon

journal homepage: www.elsevier.com/locate/carbon

Probing carrier concentration in gated single, bi- and tri-layer CVD graphene using Raman spectroscopy

Rachid Fates [a, *], Hachemi Bouridah [a], Jean-Pierre Raskin [b]

[a] Electronic Department, LEM Laboratory, Université MSB de Jijel, B.P. 98, Ouled Aissa, 18000, Jijel, Algeria
[b] Institute of Information and Communication Technologies, Electronics and Applied Mathematics, Université Catholique de Louvain, Place du Levant, 3, B-1348, Louvain-la-Neuve, Belgium

ARTICLE INFO

Article history:
Received 9 January 2019
Received in revised form
19 April 2019
Accepted 20 April 2019
Available online 21 April 2019

ABSTRACT

In this study, we experimentally investigate the evolution of the Raman spectrum of single, bi- and tri-layer graphene as function of gate voltage induced doping. In single layer graphene, the observed results are in agreement with the literature. Whereas, for bi- and tri-layer graphene, we report new results on the gate voltage induced doping dependence of G and 2D bands position, the 2D to G band intensity ratio and the G band linewidth. The gate bias through 90 nm-thick oxide allows us to move the Fermi level up to 0.43 eV and 0.31 eV for bi- and tri-layer graphene, respectively. We observe one minima in the evolution of the G band position of bilayer as function of doping. This result is explained by the presence of a larger charge density non-uniformity, which yields to electron and hole puddles in the sample. The G band position and linewidth and the 2D to G band intensity ratio show a slow variation with doping near the neutrality point, this becomes more important as doping keeps rising such as the trends present a parabolic shape dependence. We assign this to the band structure of bi- and tri-layer graphene where the carriers are massive with respect to single layer graphene.

1. Introduction

After the discovery of the two-dimensional structured carbon layers about more than fifteen years ago [1], many scientific researches were carried out on single and few-layers of graphene (GR) [2,3,4,5]. Graphene opened the field of two-dimensional systems, therefore, the outstanding physical, electrical and optical properties of graphene have been extensively studied due to the large perspectives, as well in electronic field effect devices [6,7,8,9,10], as in optic applications [11,12,13].

During the lightning evolution of graphene, a particular attention has been paid to the study of its electronic properties [14], in order to well-understand the electrical behavior of the material and thus the based-devices. Thereby, the study of the electronic properties of graphene on a conventional supporting silicon dioxide (SiO_2) on silicon (Si) substrate has attracted more interests, in particular the investigation of the charge carrier's concentration (or doping) that can directly influence the performance and reliability of the devices [15,16].

Raman spectroscopy has been the leading technique to study and characterize graphene and its derivatives, basically because it is a well-controlled, simple and non-destructive technique. In addition, because of carbon atoms are light and the sp^2 σ bonds are strong, these structural characteristics are responsible for many properties of the sp^2-bonded carbon-atoms that contribute to the high degree of sensitivity observed in Raman spectra of these systems, which allows detailed analysis of these properties. [3,17]

In the literature, several studies demonstrate the Raman technique efficiency for the characterization of graphene properties. Among these properties: (i) the number of layers of graphene materials can be identified [3,18,19], (ii) the quality of the layer including disorder, types of edges, oxidation, hydrogenation and functional groups, can be assessed [17,19,20,21], (iii) the strain-stress [22] (iv) and the presence of impurities can be probed [23,24], also (v) the electron-phonon and electron-electron interactions can be studied [3]. On the other hand, beyond the structural and mechanical properties, Raman spectroscopy was revealed as a powerful method for the evaluation of some electronic properties of graphene, such that: (vi) the carrier mobility can be evaluated for the Raman active defects [19,25,26] and (vii) the carrier concentration can be estimated [27,28,29,30,31,32,33].

* Corresponding author.
E-mail address: rachid.fates@yahoo.fr (R. Fates).

https://doi.org/10.1016/j.carbon.2019.04.078
0008-6223/

Carrier concentration has a strong influence on transport properties of graphene, so, quantifying it in graphene is crucial both to gain insight in fundamental properties, and for its applications as active material in electronic devices. Raman spectra show two main bands which are called G and 2D, for active as well as silent defects [20,33]. Three main features of Raman spectra are used to determine the type and the level of doping [19,30]: (i) the position (Pos) of the G and 2D bands, (ii) the intensity (I) ratio of the 2D and G bands I(2D)/I(G) and (iii) the full width at the half maximum (FWHM) of the G band.

The basic Raman processes could explain these features. The Raman scattering on phonons is essentially determined by electrons: how they move, interfere and scatter. Thus, any electronic properties variation due to doping affects positions, widths and intensities of the Raman peaks, enabling to probe electrons via phonons [17].

The properties of bi- and tri-layer graphene have not been studied as extensively as monolayer graphene. Because of the different band structure of both bi- and tri-layer graphene compared to monolayer graphene, the contribution of the various scattering mechanisms are expected to change in these layers [34]. In addition, with a presence of perpendicular electric field, both structures develop a tunable band gap [35,36]. The possibility of having a graphene-based system with a gap is suitable for a various applications such as digital electronic and photonic applications.

Several studies [30,31,32,33] reported the influence of the back-gate voltage on Raman features of single layer graphene. It is so interesting to extend the investigation to bi- and trilayer graphene. Here, we report a direct investigation of the gate voltage induced doping influence on the Raman spectrum of single, bi- and tri-layer CVD graphene. The gate voltage through 90 nm-thick oxide allows to move the Fermi level up to 0.47 eV, 0.43 eV and 0.31 eV for single, bi- and tri-layer, respectively. We proved that the back-gate configuration shows a low charge transfer with respect to top-gate one, because of the different quality of the oxide between top and bottom gate electrodes which results in charges coming from both oxide layers. Firstly, we check the quality of graphene by Raman measurements without any electrical biasing of the sample and establish preliminary data on the Raman spectra and their features. This is particularly important when measuring Raman peaks features, since these measurements can be altered because of surface conditions and strongly depend on the experimental setup. Secondly, we perform Raman measurements with application of a gate voltage plateau between topside and backside of the sample. This work provides significant experimental results on the dependence of the Raman spectra features to the gate voltage induced doping. The change in the spectra features of single layer graphene is in agreement with the data presented in the literature. In the case of bi- and tri-layer graphene, the Raman spectra features show relevant and original trends as function of the position of the Fermi level near and/or far from the Dirac point.

2. Experimental details

2.1. Device preparation

The graphene layers were grown on the copper (Cu) foil surface by chemical vapor deposition (CVD). In this process, commercially available Cu foils of 50 μm-thick and purity 99.9% were adopted. The graphene was grown into CVD furnace, first the Cu foil were annealed during 60 min up to 1050 °C temperature with a global pressure of 750 mbar and under 200 sccm argon (Ar) atmosphere. Next, the sample was annealed at 1050 °C in a 10% hydrogen (H_2) diluted in the Ar atmosphere for 5 min to remove native oxide on the Cu surface. This was followed by the dilution of methane (CH_4) in the Ar ambient for 30 min at the same temperature. Finally, the sample was cooled down. To ensure no extra oxidation/reduction during the cooling step, the furnace is rapidly evacuated down to a pressure of 1 mbar. More details about CVD parameters can be found in Ref. [37].

The next step consisted in transferring graphene layers on top of the oxidized silicon wafer (its final substrate). This has been accomplished by the polymethyl methacrylate (PMMA) assisted transfer method. The graphene was first covered with a 250 nm-thick PMMA layer in order to rigidify it and protect it. For that purpose, a solution of PMMA was spin-coated on the Cu surface.

The PMMA/GR/Cu sample was soaked in $FeCl_3$ solution to etch copper. The PMMA/GR layer was then put into a water bath to be rinsed. The layer was thereafter transferred by fishing onto the final wafer, consisted of a conventional Si substrate covered by a 90 nm-thick thermal SiO_2. After that, the sample was directly put in an oven at 150 °C for 3 min. The first purpose of this step is to evaporate the water confined between graphene and SiO_2. It also allows to relax the PMMA/GR film to obtain a better adhesion with the SiO_2. The PMMA layer was removed in an acetone bath for 10 min, followed by a methanol bath for 10 min and deionized water bath for 15 min, to obtain GR/SiO_2/Si sample.

The final step consists in the creation of the metallic contacts. In this purpose, the gold/titanium (Au/Ti) contacts; with 100 nm- and 10 nm-thick, respectively, were deposited in a four-corner geometry by thermal evaporation. The device fabrication process is summarized in Fig. 1. A photograph of the fabricated device with several topside contacts is shown in Fig. 2(a). A scanning electron microscopy (SEM) picture together with optical microscopy image are given in Fig. 2(b)–(c). The transferred graphene presents millimeter size single crystals of single layer (SL) graphene with a few multilayer (ML) regions similarly to what is produced in Ref. [38].

2.2. Characterization technique

The Raman spectra were acquired with a micro-Raman spectroscopy (LabRAM HR Horiba), equipped with a micrometer multi-axis stage and a thermal stage (HFS600E-PB4 thermal probe stage). The Raman spectra were collected with a ×50 objective using a laser excitation wavelength of 514.5 nm (the excitation energy is 2.41 eV). A 2400 grooves/mm grating is used in order to obtain precise values of the peaks positions and FWHM. The laser spot size is estimated to be ~1 μm and the incident power is kept well below 1 mW using a 1% power filter in order to avoid damage or heating effects. The data was analyzed using LabSpec software. Metallic needles were positioned to probe the topside contact and the back-gate contact as described in Fig. 2(d), in order to perform Raman analysis with applying voltage.

3. Results and discussion

Raman measurements in absence of gate voltage were performed on single layer (SLG), bilayer (BLG) and trilayer graphene (TLG), as shown in Fig. 3(a)–(b). This action aims to both check the quality of the transferred graphene and establish preliminary data on the Raman spectra and their features, i.e. the I(2D)/I(G) ratio, the positions of G and 2D bands and the FWHM of the G band. These results are plotted in Fig. 3(c)–(e).

In Fig. 3(a), the Raman spectra show G peak (around 1590 cm^{-1}) and 2D peak (around 2690 cm^{-1}) for SLG, BLG and TLG. We observe that the spectra intensity decreases from SLG to TLG. The main apparent difference between the three structures is the sensitivity of the 2D peak intensity to the number of graphene stacked-layers. Concerning the G peak, the intensity presents a less important sensitivity and decreases slowly from SLG to TLG. On the other

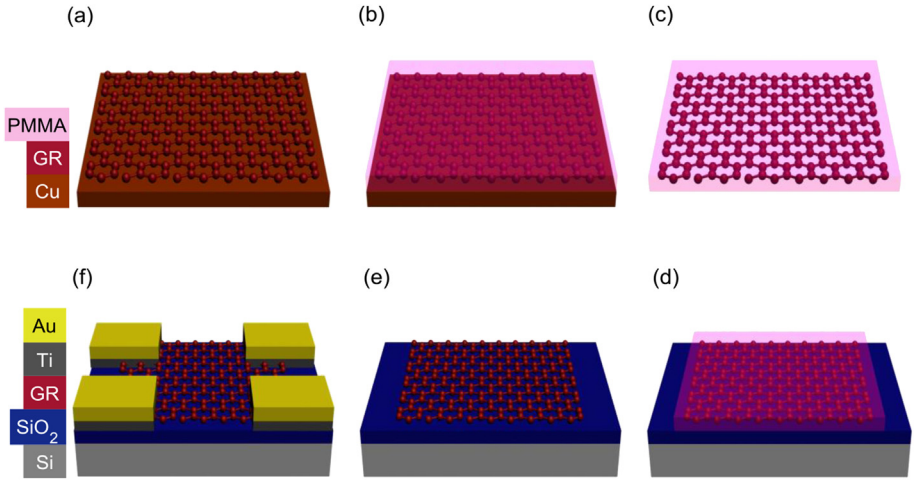

Fig. 1. Schematic illustration of the device fabrication using the SiO_2/Si supported graphene and Au/Ti electrodes. **(a)** CVD graphene is prepared on Cu foil. **(b)** A layer of PMMA is spin-coated on the graphene face. **(c)** Cu foil is etched away using $FeCl_3$ solution to obtain free-standing PMMA/GR layer. **(d)** PMMA/GR layer is transferred to the SiO_2/Si wafer. **(e)** The PMMA layer is removed. **(f)** Au/Ti electrodes are deposited on the four corners of the GR/SiO_2/Si sample.

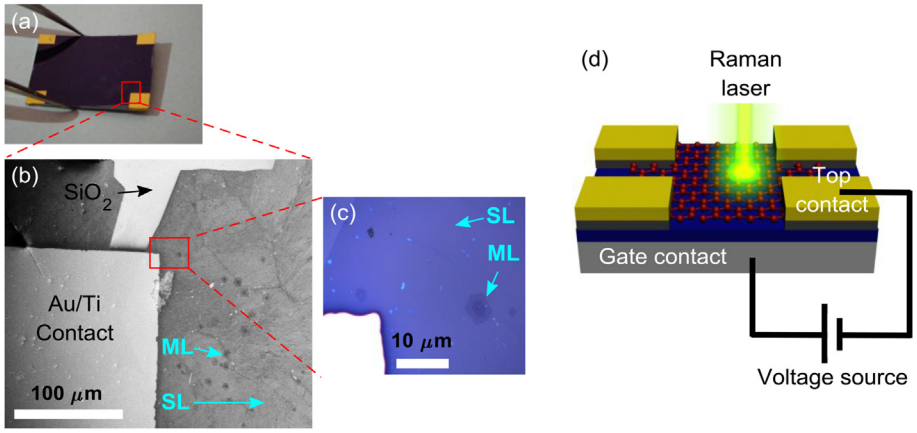

Fig. 2. Description of the measured device. **(a)** Photograph of the fabricated device. **(b)** SEM image of the location denoted in panel **a** showing: the transferred graphene on 90 nm-thick SiO_2, single layer graphene domains and localized multilayer graphene domains. **(c)** Optical microscopy image of the location denoted in panel **b**. **(d)** Schematic illustration of the Raman measurements setup.

hand, the D peak was not observed in all the measurements. The absence of D band indicates the graphene is largely defect free. As reported in Refs. [20,33], the absence of D peak could indicates that the graphene has perfect zigzag edges or charged impurities. In Fig. 3(c)–(d), from TLG to SLG, the G peaks as well as 2D peaks show a change in position of 3–6 cm^{-1}. However, the relative intensity of the 2D to G peak ratio significantly varies in SLG (from 2.3 to 2.8) with respect to BLG (from 0.86 to 0.94) and TLG (from 0.63 to 0.74).

In the literature, BLG is classified into two categories. The first one is the AB-stacked, where the two graphene layers are such that the A-triangular sub-lattice of the top (bottom) layer lies exactly on top of the B-sub-lattice of bottom (top) layer. The second category where the two atomic layers planes are rotated relative to each other is often referred to as turbostratic, misoriented, or twisted BLG [39,40,41,42,43]. The twist angle of BLG can be determined using the transmission electron microscopy (TEM) analysis [39]. Nevertheless, this method is very complicated because it involves the transfer of the BLG on a TEM grid. A second method, consisting in the measuring of the angles formed between neighboring edges of the first and the second layer [40]. This method is not very efficient because of the first layer is almost millimeter-size and the second one is micrometer-size. A third method consists in the use of Raman bands features to estimate the twist angle between two stacked layers. It has been shown that the Raman low energy modes [40], the line width of 2D band and the 2D to G band intensity ratio [41] change as a function of twisting angle. The change in low energy modes with respect to twist angle is relatively small except for the critical angles [39,40], thus the extraction of the twist angle based on the low frequency modes is not really accurate. The change in Raman 2D band FWHM exhibits a very complex rotational angle dependence. Indeed, the twist angle does not change monotonically between 0° and 10°. First, a decrease in FWHM(2D) was observed from 0° to 5°, then, at around 7°–9°, an increase in FWHM(2D) was observed [41], while a decrease appears for angles larger than 10°. For example, as reported in Ref. [41], both angle ranges 0°–1° (AB-stacked) and 8°–9° exhibit a same FWHM(2D) of 55–60 cm^{-1}. Moreover, other values have been reported in the literature, such as the 2D band FWHM for AB-stacked can vary from 38 to 46 cm^{-1} [44]. In summary, the 2D band FWHM is not an accuracy feature to estimate the twist angle in BLG. In this work, we adopted another Raman feature consisting in estimating the twist angle from the 2D to G band intensity ratio [40,41]. Unlike the line width, the 2D to G band intensity ratio is extremely angle dependent, because the 2D to G band intensity ratio implies both the G

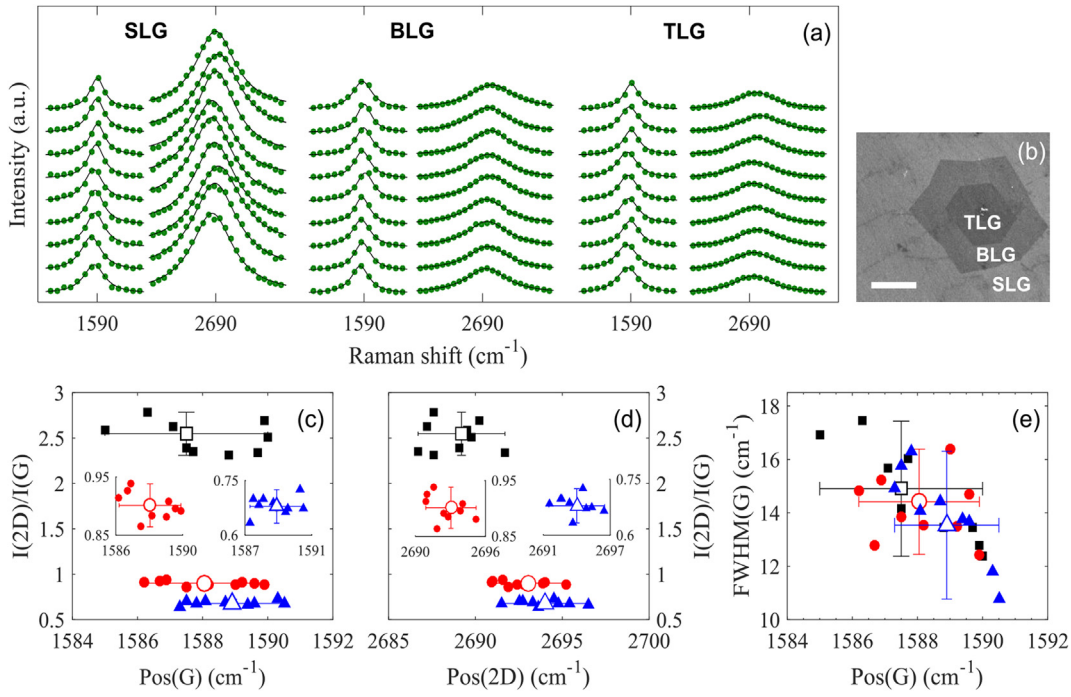

Fig. 3. Raman characterization of SLG, BLG and TLG without any basing of the sample. **(a)** Comparison of Raman spectra at nine different locations in SLG, BLG and TLG. Dots are the measurements and lines are the Lorentzian fits to data. **(b)** SEM picture showing the regions where the data of panel **a** was measured. Scale bar: 2 μm. **(c)** and **(d)** present the measurements of I(2D)/I(G) ratio as function of Pos(G) and Pos(2D), respectively. Squares indicate SLG; circles indicate BLG; and triangles indicate TLG. **(e)** The FWHM(G) measurements as function of Pos(G).

and 2D bands intensities, which gives a more precise twist angle estimation. It was demonstrated that I(2D) decreases with respect to I(G) as the twist angle increases from 0° (AB-stacked) to a critical angle of about 10°–13° [40,41]. Beyond the critical angle (14°–30°), I(2D) rapidly increases such as BLG displays Raman spectra similar to those of SLG [41,42], and the electronic properties of the twisted layers become indistinguishable from SLG, this is reflected on the Raman spectrum by I(2D)/I(G) ≫ 1. While, several studies [44,45,46,47] reported that I(2D)/I(G) ~ 1 is characteristic of AB-stacked (Bernal) bilayer graphene. From the results shown in Fig. 3(c)–(d) and Fig. 8(a) (near Dirac point), I(2D)/I(G) ~ 1. Therefore, we conclude that the observed BLG sample is in the AB stacking. Concerning TLG, the literature [48,49,50] reports that two crystalline forms are possible: Bernal (ABA) and rhombohedral (ABC) stacking orders, and both stacking orders display I(2D)/I(G) ≪ 1. In the case of TLG, the 2D band FWHM can give information about the stacking order [48]. For excitation energy of 2.33 eV and 2.4 eV, the FWHM(2D) for ABA stacking can vary in the range of 40–60 cm^{-1}, whereas, for ABC stacking the FWHM(2D) is wider than 60 cm^{-1} [48,49,50]. In our experiments, the TLG samples exhibit a FWHM(2D) in the range of 38–48 cm^{-1}, therefore we can conclude that our TLG samples are ABA-stacked structures. Beside this, the relative intensity of the 2D to G peak ratio observed in Fig. 3(c)–(d) decreases when the number of layers increases, which is consistent with the result observed in Ref. [51].

Fig. 3(e) shows the FWHM(G) as function of Pos(G). The FWHM(G) decreases from SLG to TLG similar to intensity. There is a clear correlation: a Pos(G) upshift (downshift) induces a FWHM(G) decrease (increase). Fig. 3(c)–(e) indicates that the G and 2D peaks can be sometimes asymmetric. Note that these results do not mean that the Raman spectra always vary in different regions within a given sample. However, it warns that the graphene uniformity has to be checked, and cannot be simply assumed.

3.1. Single layer graphene

Here, we focus on the effect of the back-gate voltage on doping concentration in SLG. Fig. 4(a) plots Raman spectra of SLG for a gate voltage ranging from −40 to 50 V. The G peak downshifts from −40 to 15 V then upshifts beyond 15 V. Regarding 2D peak, spectra downshift with increasing the gate voltage.

In order to evaluate the carrier concentration in SLG, it is necessary to convert the back-gate voltage into an effective charge carrier concentration. The application of gate voltage (V_G) creates an electric field through the gate oxide and induces a charge concentration in graphene. Electron (hole) charge concentration induced by positive (negative) V_G can be modulated according to the relation [52,53]

$$n = n_e - n_h = \frac{V_G - V_{Dirac}}{e}\left(\frac{1}{C_{ox}} + \frac{1}{C_q}\right)^{-1} \quad (1)$$

where n_e (n_h) is the electron (hole) charge concentration, V_{Dirac} is the gate voltage corresponding to the charge neutrality point (or Dirac point), e is the electron charge, $C_{ox} = \varepsilon_{ox}/t_{ox}$ is the gate oxide capacitance, ε_{ox} is the relative dielectric constant, t_{ox} is the gate oxide thickness and C_q is the quantum capacitance. SLG has zero band gap and the charge carriers are massless quasiparticles with a linear dispersion, so, the quantum capacitance is $C_q = 2E_F e^2/\pi(\hbar v_F)^2$ [52], where the Fermi energy E_F is function of n and changes as [54]

$$E_F = sign(n)\hbar v_F\sqrt{\pi|n|}, \quad (2)$$

$\hbar$ is the reduced Planck constant, v_F is the Fermi-Dirac velocity (= 1.1×10^6 m/s) and $sign(n)$ is positive (negative) for electrons (holes) and changes at $V_G = V_{Dirac}$. Using numerical values, for $t_{ox} = 90$ nm, C_q ~10^{-6} F/cm^2 and C_{ox} ~10^{-8} F/cm^2. Therefore, it is clear that $C_q \gg C_{ox}$. In addition, when the Fermi level is located

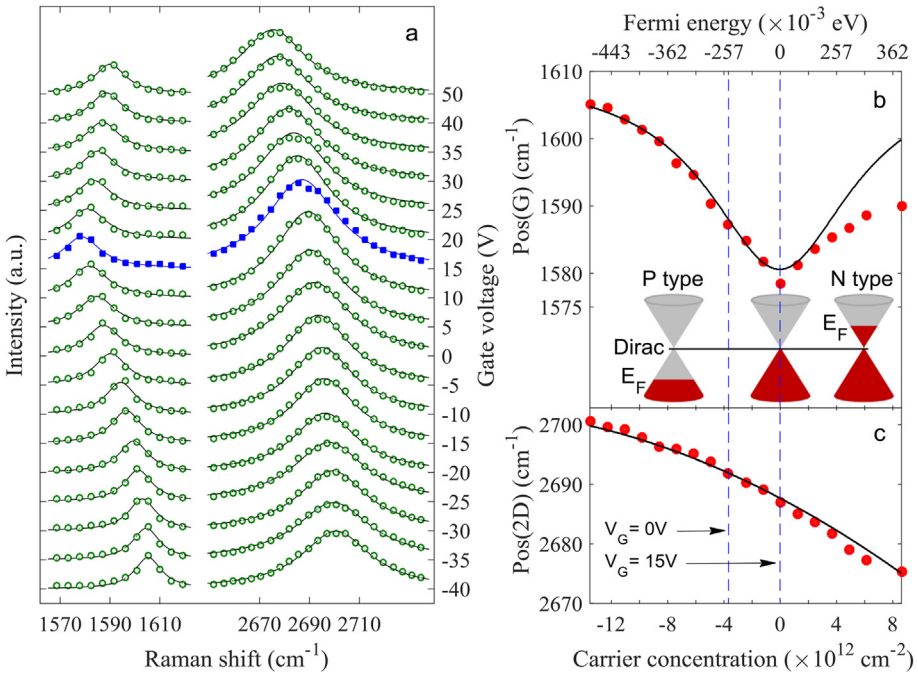

Fig. 4. Dependence of Raman spectra of SLG on back-gate voltage. **(a)** Raman spectra for a gate voltage ranging from −40 to 50 V. Symbols are the measurements and the solid lines are Lorentzian fits. The blue spectrum (denoted with squares) highlights the minimum shift of the G band which corresponds to the spectrum at the Dirac point ($V_G = V_{Dirac} = 15$ V). **(b)** Dependence of Pos(G) on carrier concentration (bottom axis) and Fermi energy (top axis). Dots are the measurements and the solid line is a Lorentzian fit. The band structure shows the location of the Fermi level. The spectrum at $V_G = 0$ V corresponds to a hole concentration of 3.7×10^{12} cm^{-2} and a Fermi energy of 0.24 eV below the Dirac level. **(c)** Dependence of Pos(2D) on carrier concentration (bottom axis) and Fermi energy (top axis). Dots are the measurements and the solid line is a fit.

above or below Dirac level, only electrons or holes are present. Consequently, equation (1) can be reduced to $n = C_{ox}(V_G - V_{Dirac})/e$.

Fig. 4(b) plots Pos(G) as a function of E_F and n. The Pos(G) is directly related to the carrier concentration and the Fermi energy, which are controlled by the applied gate voltage. The minimum value of Pos(G) is reached at the charge neutrality point situated near $V_G = V_{Dirac} = 15$ V. When E_F moves from V_{Dirac}, the G peak upshifts for both electron (positive n and E_F) and hole (negative n and E_F) doping. The variation of Pos(G) with E_F is due to the nonadiabatic removal of the Kohn anomaly [31,55]. We notice an asymmetry of the Pos(G) measurements between the valence and conduction bands, indeed, the Pos(G) measurements show an excellent agreement with a Lorentzian fit for holes concentration, while for electrons concentration the measurements show a different trend from the fit. This shows that the G phonon energy is different for hole and electron doping. In Fig. 4(c), the dependence of Pos(2D) on E_F is different from that of Pos(G). Indeed, physically the 2D peak originates from a second-order, double-resonant Raman scattering mechanism, whereas the G peak is due to the doubly degenerate zone center E_{2g} mode [18]. Experimentally, this gives a decrease of Pos(2D) when E_F keeps rising from valence band to conduction band, i.e. the decrease of the Pos(2D) takes place with the decrease of hole concentration close to charge neutrality point and the increase of electron concentration. The variation of the 2D peak with doping is mainly due to a modification of the lattice parameters caused by doping, which changes the total number of charges [33]. On the other hand, we notice that Pos(G) and Pos(2D) present similar trends for hole-doping (p-type) and opposite trends for electron-doping (n-type). This is used to distinguish hole doping from electron doping using Raman spectroscopy. The change of the Fermi energy in gated graphene induced by doping has a significant effect on the equilibrium lattice parameters, which results in a stiffening or softening of the phonons [30].

Fig. 5(a) plots I(2D)/I(G) in SLG as a function of E_F and n. We observe a large variation with carrier concentration: the 2D peak is 1.8–2.8 times stronger than the G peak. The intensity ratio is fitted by a Lorentzian shape, it reaches a maximum value at the Dirac point. When E_F moves from Dirac point, I(2D)/I(G) decreases. In Fig. 5(b), I(G) and I(2D) as function of n show clearly that I(G) is insensitive to changes in carrier concentration, whereas I(2D) strongly decreases for increasing carrier concentration. When E_F increases, the I(2D) decreases due to the effect of increased electron-electron interactions, which results in I(2D)/I(G) decrease [56]. This is consistent with the results of Refs. [31,33].

Fig. 6 shows that the FWHM(G) is very sensitive to carrier concentration. Indeed, when the carrier concentration increases (decreases), the G band narrows (broadens). Similar to I(2D)/I(G) in Fig. 5(a), the FWHM(G) reaches a maximum at neutrality point and it varies like a Lorentzian shape. The reduction of the G bandwidth at higher carrier densities is due to Pauli exclusion principle inhibiting phonon decay into electron-hole pairs when E_F surpasses half of the phonon energy [28,33].

The results presented in Fig. 4–6 are consistent with the observed results in Refs. [30,33], and have similar trends to those obtained for different laser wavelengths: 532 nm [29] and 633 nm [33]. Beside this, the back-gate configuration presents low doping with respect to top-gate configuration [30,33] because of the different quality of the oxide between top and bottom gate electrodes.

3.2. Bilayer and trilayer graphene

Fig. 7(a) shows BLG Raman spectra for the gate voltage ranging from −40 to 50 V. The G peak downshifts with increasing V_G up to 15 V, and then upshifts beyond. Concerning the 2D peak, spectra downshift with increasing V_G.

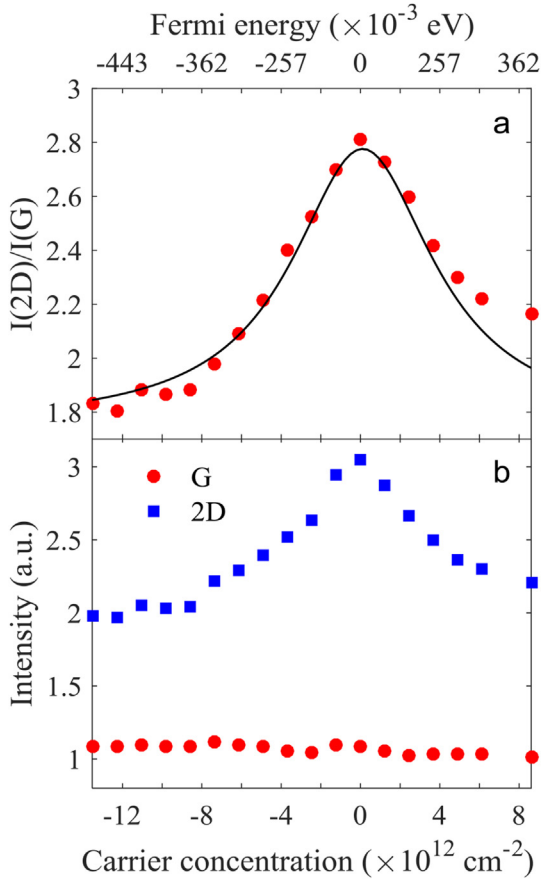

Fig. 5. Intensity of the G and 2D peaks in SLG as function of Fermi energy (top axis) and carrier concentration (bottom axis). **(a)** I(2D)/I(G). **(b)** Details of I(G) and I(2D). Dots are the measurements and the solid line is a Lorentzian fit.

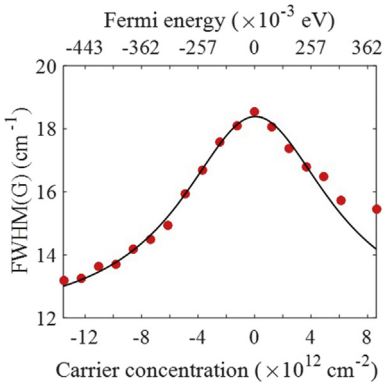

Fig. 6. Dependence of FWHM(G) on Fermi energy and carrier concentration. Dots are measurements and solid line is a Lorentzian fit.

As shown for SLG, the back-gate voltage has to be converted into an effective carrier concentration and equivalent Fermi energy in BLG and TLG. For this purpose, equation (1) can be used in BLG and TLG except that the quantum capacitance is $C_q = 2me^2/\pi\hbar^2$ [52], where m is the carrier effective mass. The effective mass is defined as function of the electron mass m_0 such as $m = 0.037m_0$ and $m = 0.052m_0$ [52,57] for BLG and TLG, respectively.

AB-stacked BLG and TLG in its ABA- and/or ABC-stacking orders have a parabolic band structure (quadratic dispersion), thus, the Fermi energy is given as follow [52]

$$E_F = \frac{\hbar^2 \pi n}{2m} \tag{3}$$

Using numerical values, we find $C_q \sim 10^{-6}$ F/cm^2 and C_{ox} is unchanged. Therefore, it is clear that $1/C_q \ll 1/C_{ox}$, thus equation (1) can be reduced as shown for SLG. Note that in BLG and TLG, C_q and E_F are function of m, and E_F is proportional to n, while in SLG where the charge carriers are massless, C_q is function of E_F which is proportional to $n^{0.5}$.

Fig. 7(b)–(c) show the dependence of Pos(G) and Pos(2D) on carrier concentration and Fermi level. While the observed Pos(2D) evolution in BLG is similar to that of SLG, change in the Pos(G) is rather different. In BLG, the Pos(G) shows one minimum value at charge neutrality point, which corresponding to a G band position of 1582.5 cm^{-1} and a G phonon energy of 196.2 meV. When charge carriers are added into BLG by electric field effect, the G band position/energy increases. However, similar n results in much smaller E_F, because of E_F changes much slower with n than in SLG, this is linked to the difference in the band structure, and also the fact that the carriers are massive in BLG and massless in SLG. Besides this, the measurements shown in Fig. 7(b) present a good agreement with a parabolic fit with respect to those observed in SLG. These results show that the position of the G band depends on the gate voltage, which is consistent with the observed results in back-gated BLG [58], as well as in top-gated BLG [59,60]. Furthermore, in our experiment we observe only one minima at the charge neutrality point, unlike to the results of Refs. [58,59] where the splitting of the G band as function of doping is observed, giving the so-called phonon anomaly. The result shown in Fig. 7(b) can be explained by the presence of a larger charge density non uniformity, which yields to electron and hole puddles in the graphene [58,61]. The results observed in Fig. 7 show a low charge transfer with respect to top-gated BLG [59,60]. The reason is that the different quality of the oxide between top and bottom gate electrodes results in charges coming from both oxide layers.

Another important point is that the G band energy change with Fermi energy is slow around the charge neutrality point. Indeed, for $|E_F| < \sim 0.115$ eV, the measurements show an evolution of the G band energy of ~2 cm^{-1} as well for electron as for hole doping. For $|E_F| > \sim 0.115$ eV, we observe faster change, which shows a pronounced gate tunability. Under perpendicular applied electric field effect, BLG should be a tunable-gap semiconductor [62], in other words the broadening of the band gap is field effect dependent. Therefore, the slow evolution around the neutrality point, shown in Fig. 7(b), is attributed to the band structure of BLG where the carriers are massive with respect to SLG, and could be related to an opened band gap when V_G moves from V_{Dirac}. As E_F increases, the induced band gap can be continuously tuned close to saturation. Experimentally the band gap in BLG were been observed with a continuous broadening up to 0.25 eV [35]. In Fig. 8(a), I(2D)/I(G) ratio in BLG varies as a parabolic shape with doping, it reaches a maximum value at the charge neutrality point and decreases as the doping increases. Moreover, in Fig. 8(b), the I(2D) is very sensitive to change in carrier concentration, whereas I(G) has no doping dependence. The trends of I(2D)/I(G) versus doping in Figs. 8(a) and 5(a) are almost similar, this implies that these features share a common origin. Therefore, the decrease of I(2D)/I(G) when the doping increases is attributed to the I(2D) decrease due to the effect of increased electron-electron interactions [56]. This result shows that the coupling between the two layers does not prevent the effect of increased electron-electron interactions on 2D band intensity. The FWHM(G) as function of E_F and n is plotted in Fig. 8(c). The FWHM(G) measurements show a good agreement with parabolic fit with a

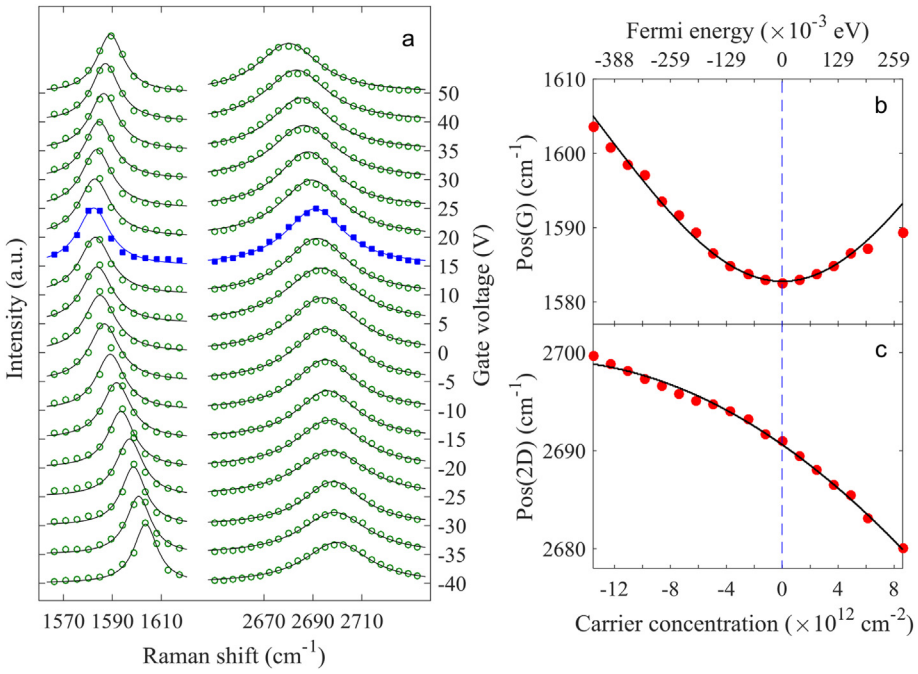

Fig. 7. Dependence of Raman spectra of BLG on back-gate voltage. **(a)** Raman spectra for V_G in the range from −40 to 50 V. Symbols are the measurements (Squares correspond to Dirac point) and solid lines are Lorentzian fits. Dependence of **(b)** Pos(G) and **(c)** Pos(2D) on carrier concentration (bottom axis) and Fermi energy (top axis). Dots are the measurements and solid lines are fits.

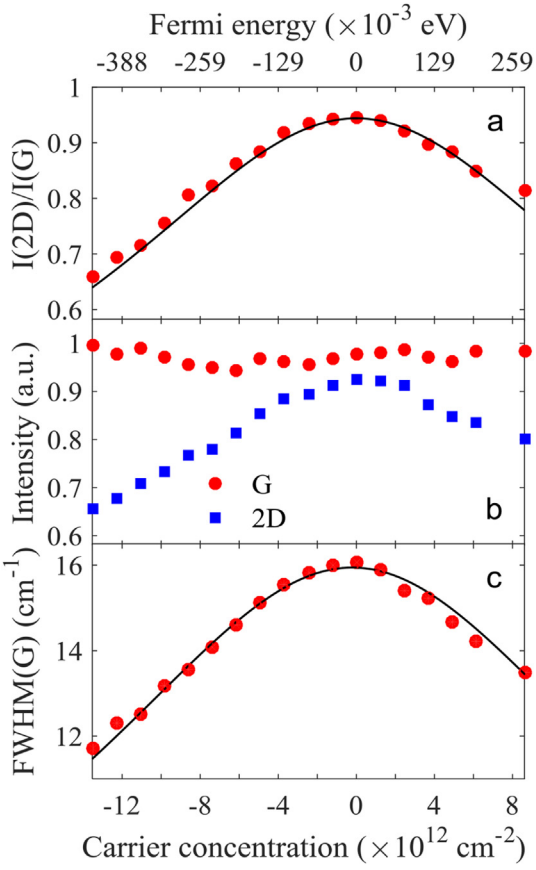

Fig. 8. Dependence of **(a)** I(2D)/I(G), **(b)** I(G) and I(2D) and **(c)** FWHM(G) on carrier concentration in BLG. Symbols are the measurements and the solid lines are parabolic fits.

maximum value at neutrality point. An increase in either electron or hole density increases the phonon lifetime due to the inhibition of the process of phonon decay into electron-hole pairs, which reduces the FWHM(G).

In Fig. 9(a), the Raman spectra collected on TLG show the same trends about G and 2D bands than BLG. Moreover, the charge neutrality point in located at $V_G = 15$ V. We notice in Fig. 9(b)–(c) that the Fermi level changes much slower with n than in BLG, because of the carrier effective mass is bigger, i.e. $m_{TLG} = 0.052m_0$ versus $m_{BLG} = 0.037m_0$. Fig. 9(b) shows a slow change (~1.2 cm^{-1}) of the Pos(G) in TLG for $|E_F| < 0.085$ eV. For $|E_F| > 0.085$ eV, we observe an important variation as well for electron doping as for hole doping. As reported in Ref. [36], the energy gap of TLG shows a dependence on the field effect induced doping. A quantitative understanding requires to consider the theory of TLG band structure [36]. Therefore, the slow evolution observed in Fig. 9(b) is assigned to the band structure of TLG together with BLG where the carriers are massive with respect to single layer graphene, this could be related to the presence of a band gap when V_G is near to V_{Dirac}. Regarding to 2D band, Fig. 9(c) shows a change of ~14 cm^{-1} in Pos(2D) (versus ~20 cm^{-1} in BLG) for a gate voltage ranging from −40 to 50 V.

In Fig. 10(a), while I(2D)/I(G) ratio in TLG is weaker than in BLG, it varies as a parabolic shape with doping. Fig. 10(b) shows that I(2D) and I(G) have similar dependence to doping with respect to BLG. In addition, albeit the doping changes, I(2D) in TLG is weaker than I(2D) in BLG. This result shows that the sensitivity of I(2D) to the number of graphene stacked-layers is independent on doping, which is in line with the results shown in Fig. 3. The dependence of FWHM(G) on doping in TLG is shown in Fig. 10(c). The FWHM(G) shows similar trend to that observed in BLG with a change between ~11.2 cm^{-1} and ~14.6 cm^{-1} (versus ~11.8 cm^{-1} and ~16 cm^{-1} in BLG). Fig. 9–10 show that TLG Raman spectra features have similar trends to those of BLG in: (i) G and 2D bands position, (ii) G and 2D bands intensity and (iii) G band FWHM. The reason is that TLG as

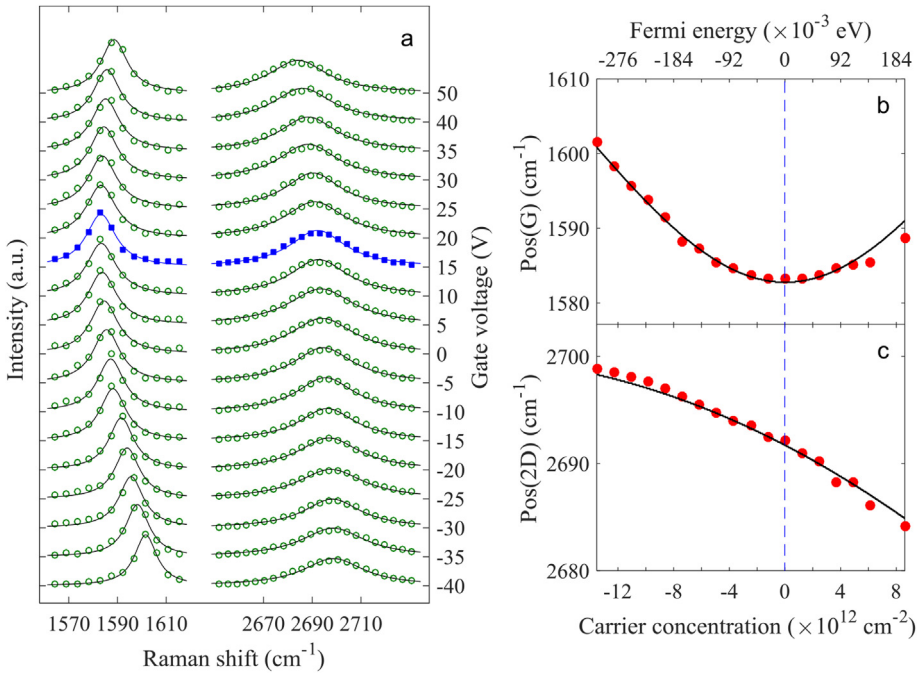

Fig. 9. Dependence of Raman spectra of TLG on back-gate voltage. **(a)** Raman spectra for V_G in the range from −40 to 50 V. Symbols are the measurements (squares correspond to Dirac point) and solid lines are Lorentzian fits. Dependence of **(b)** Pos(G) and **(c)** Pos(2D) on carrier concentration (bottom axis) and Fermi energy (top axis). Dots are the measurements and solid lines are fits.

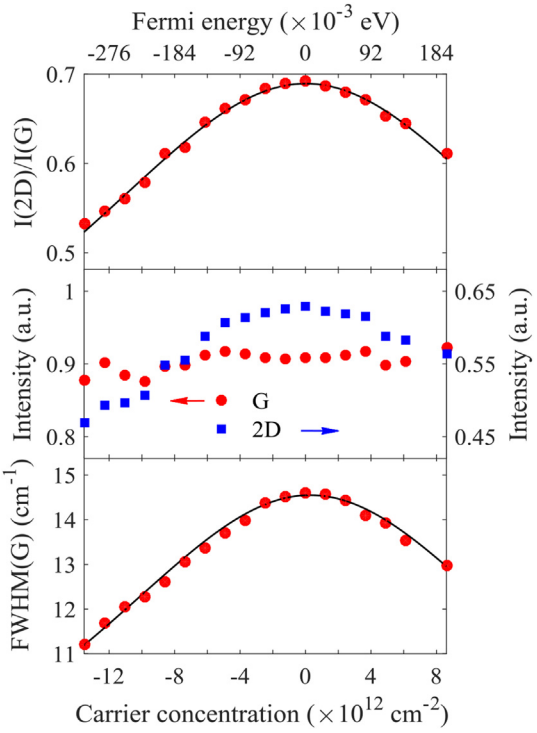

Fig. 10. Dependence of **(a)** I(2D)/I(G), **(b)** I(G) and I(2D) and **(c)** FWHM(G) on carrier concentration in TLG. Symbols are the measurements and the solid lines are parabolic fits.

well as BLG have: (i) a parabolic band structure, (ii) a band gap tuned with doping and (iii) another important point is that the electrons and holes are not only chiral but also massive compared to SLG.

4. Conclusion

In conclusion, we studied the change of the Raman spectroscopy signal with varying applied voltage in gated SLG, BLG and TLG. We proved that the gate voltage through 90 nm-thick oxide allows moving the Fermi level up to 0.47 eV, 0.43 eV and 0.31 eV for SLG, BLG and TLG, respectively. In SLG, Raman spectra features show a Lorentzian dependence to the Fermi level. In the case of BLG and TLG, Raman spectra features show a parabolic dependence to the gate voltage induced doping, such that when doping increases: (i) the G band position increases and linewidth narrows, (ii) the 2D band position increases for p-doping and decreases for n-doping and (iii) the 2D band intensity decreases. In BLG, we observe one minima in the evolution of the G band position as function of doping. This is caused by the presence of a larger charge density non-uniformity, which yields to electron and hole puddles in the sample. Moreover, we proved that the back-gate configuration shows a low charge transfer with respect to top-gate one, because of the different quality of the oxide between top and bottom gate electrodes which results in charges coming from both oxide layers. The Raman spectra features in BLG and TLG show a slow evolution when the Fermi level is near/around the neutrality point, we assign this to the band structure of bi- and tri-layer graphene where the carriers are massive with respect to single layer graphene. The dependence of the Raman spectra of single, bi- and tri-layer graphene on doping makes Raman spectroscopy a reliable tool for analyzing the electronic properties of single and multilayer graphene devices.

Acknowledgement

The authors would like to acknowledge the Action de Recherche Concertée (ARC) “Naturist” project granted by the Communauté fançaise de Belgique for their financial support. We also acknowledge Wallonia Infrastructure for Nano FABrication (WINFAB) and

Wallonia ELectronics and COmmunication MEasurements (WELCOME) for electrical and Raman measurements. Particular thanks to Dr. Benjamin Huet for graphene synthesis and Ferran Urena for Raman system training, as well as their very useful scientific pieces of advice.

References

[1] K.S. Novoselov, A.K. Geim, S.V. Morozov, D. Jiang, Y. Zhang, S.V. Dubonos, I.V. Grigorieva, A.A. Firsov, Electric field effect in atomically thin carbon films, Science 306 (2004) 666–669.
[2] A.K. Geim, K.S. Novoselov, The rise of graphene, Nat. Mater. 6 (2007) 183–191.
[3] L.M. Malard, M.A. Pimenta, G. Dresselhaus, M.S. Dresselhaus, Raman spectroscopy in graphene, Phys. Rep. 473 (2009) 51–87.
[4] C.-J. Shih, A. Vijayaraghavan, R. Krishnan, R. Sharma, J.-H. Han, M.-H. Ham, Z. Jin, S. Lin, G.L.C. Paulus, N.F. Reuel, Q.H. Wang, D. Blankschtein, M.S. Strano, Bi- and trilayer graphene solutions, Nat. Nanotechnol. 6 (2011) 439–445.
[5] K. Tsukagoshi, S.-L. Li, H. Miyazaki, A. Aparecido-Ferreira, S. Nakaharai, Semiconducting properties of bilayer graphene modulated by an electric field for next-generation atomic-film electronics, J. Phys. D Appl. Phys. 47 (2014) 094003.
[6] F. schwierz, Graphene transistors, Nat. Nanotechnol. 5 (2010) 487–496.
[7] S. Bae, H. Kim, Y. Lee, X. Xu, J.S. Park, Y. Zheng, J. Balakrishnan, T. Lei, H.R. Kim, Y.I. Song, Y.-J. Kim, K.S. Kim, B. Özyilmaz, J.-H. Ahn, B.H. Hong, S. Iijima, Roll-to-roll production of 30-inch graphene films for transparent electrodes, Nat. Nanotechnol. 5 (2010) 574–578.
[8] O. Moldovan, B. Iiguez, M.J. Deen, L.F. Marsal, Graphene electronic sensors – review of recent developments and future challenges, IET Circuits, Devices Syst. 9 (2015) 446–453.
[9] P. Avouris, Graphene: electronic and photonic properties and devices, Nano Lett. 10 (2010) 4285–4294.
[10] S.Z. Butler, S.M. Hollen, L. Cao, Y. Cui, J.A. Gupta, H.R. Gutierrez, T.F. Heinz, S.S. Hong, J. Huang, A.F. Ismach, E. Johnston-Halperin, M. Kuno, V.V. Plashnitsa, R.D. Robinson, R.S. Ruoff, S. Salahuddin, J. Shan, L. Shi, M.G. Spencer, M. Terrones, W. Windl, J.E. Goldberger, Progress, challenges, and opportunities in two-dimensional materials beyond graphene, ACS Nano 7 (2013) 2898–2926.
[11] J. Wei, Z. Zang, Y. Zhang, M. Wang, J. Du, X. Tang, Enhanced performance of light-controlled conductive switching in hybrid cuprous oxide/reduced graphene oxide (Cu_2O/rGO) nanocomposites, Optic Lett. 42 (2017) 911–914.
[12] Z. Zang, X. Zeng, M. Wang, W. Hu, C. Liu, X. Tang, Tunable photoluminescence of water-soluble AgInZnS-graphene oxide (GO) nanocomposites and their application in-vivo bioimaging, Sensor. Actuator. B Chem. 252 (2017) 1179–1186.
[13] X. Liu, T. Xu, Y. Li, Z. Zang, X. Peng, H. Wei, W. Zha, F. Wang, Enhanced X-ray photon response in solution-synthesized $CsPbBr_3$ nanoparticles wrapped by reduced graphene oxide, Sol. Energy Mater. Sol. Cell. 187 (2018) 249–254.
[14] A.H.C. Neto, F. Guinea, N.M.R. Peres, K.S. Novoselov, A.K. Geim, The electronic properties of graphene, Rev. Mod. Phys. 81 (2009) 109–162.
[15] R. Fates, J.-P. Raskin, Linear and non-linear electrical behaviors in graphene ribbon based devices, J. Sci.: Advanced Materials and Devices 3 (2018) 366–370.
[16] P. Aydogan, N. Kakenov, C. Kocabas, S. Suzer, Raman and X-Ray photoelectron spectroscopic studies of graphene devices for identification of doping, Appl. Surf. Sci. 425 (2017) 1130–1137.
[17] A.C. Ferrari, D.M. Basko, Raman spectroscopy as a versatile tool for studying the properties of graphene, Nat. Nanotechnol. 8 (2013) 235–246.
[18] A.C. Ferrari, J.C. Meyer, V. Scardaci, C. Casiraghi, M. Lazzeri, F. Mauri, S. Piscanec, D. Jiang, K.S. Novoselov, S. Roth, A.K. Geim, Raman spectrum of graphene and graphene layers, Phys. Rev. Lett. 97 (2006) 187401.
[19] B. Tang, H. Guoxin, H. Gao, Raman spectroscopic characterization of graphene, Appl. Spectrosc. Rev. 45 (2010) 369–407.
[20] L.G. Cançado, A. Jorio, E.H. Martins Ferreira, F. Stavale, C.A. Achete, R.B. Capaz, M.V.O. Moutinho, A. Lombardo, T.S. Kulmala, A.C. Ferrari, Quantifying defects in graphene via Raman spectroscopy at different excitation energies, Nano Lett. 11 (2011) 3190–3196.
[21] R. Beams, L.G. Cançado, L. Novotny, Raman characterization of defects and dopants in graphene, J. Phys. Condens. Matter 27 (2015) 083002.
[22] M. Huang, Y. Hugen, T.F. Heinz, J. Hone, Probing strain induced electronic structure change in graphene by Raman spectroscopy, Nano Lett. 10 (2010) 4074–4079.
[23] C. Casiraghi, S. Pisana, K.S. Novoselov, A.K. Geim, A.C. Ferrari, Raman fingerprint of charged impurities in graphene, Appl. Phys. Lett. 91 (2007) 233108.
[24] R. Cunha, N. Perea-López, A.L. Elías, K. Fujisawa, V. Carozo, S. Feng, R. Lv, M.C. dos Santos, M. Terrones, P.T. Araujo, Probing the interaction of noble gases with pristine and nitrogen-doped graphene through Raman spectroscopy, Phys. Rev. B 97 (2018) 195419.
[25] J.A. Robinson, M. Wetherington, J.L. Tedesco, P.M. Campbell, X. Weng, J. Stitt, M.A. Fanton, E. Frantz, D. Snyder, B.L. VanMil, G.G. Jernigan, R.L. Myers-Ward, C.R. Eddy Jr., D.K. Gaskill, Correlating Raman spectral signatures with carrier mobility in epitaxial graphene: a guide to achieving high mobility on the wafer scale, Nano Lett. 9 (2009) 2873–2876.
[26] Y.S. Woo, D.W. Lee, U.J. Kim, General Raman-based method for evaluating the carrier mobilities of chemical vapor deposited graphene, Carbon 132 (2018) 263–270.
[27] J. Yan, Y. Zhang, P. Kim, A. Pinczuk, Electric field effect tuning of electron-phonon coupling in graphene, Phys. Rev. Lett. 98 (2007) 166802.
[28] S. Pisana, M. Lazzeri, C. Casiraghi, K.S. Novoselov, A.K. Geim, A.C. Ferrari, F. Mauri, Breakdown of the adiabatic Born–Oppenheimer approximation in graphene, Nat. Mater. 6 (2007) 198–201.
[29] C. Stampfer, F. Molitor, D. Graf, K. Ensslin, A. Jungen, C. Hierold, L. Wirtz, Raman imaging of doping domains in graphene on SiO_2, Appl. Phys. Lett. 91 (2007) 241907.
[30] A. Das, S. Pisana, B. Chakraborty, S. Piscanec, S.K. Saha, U.V. Waghmare, K.S. Novoselov, H.R. Krishnamurthy, A.K. Geim, A.C. Ferrari, A.K. Sood, Monitoring dopants by Raman scattering in an electrochemically top-gated graphene transistor, Nat. Nanotechnol. 3 (2008) 210–215.
[31] C. Casiraghi, Doping dependence of the Raman peaks intensity of graphene close to the Dirac point, Phys. Rev. B 80 (2009) 233407.
[32] Z.H. Ni, T. Yu, Z.Q. Luo, Y.Y. Wang, L. Liu, C.P. Wong, J. Miao, W. Huang, Z.X. Shen, Probing charged impurities in suspended graphene using Raman spectroscopy, ACS Nano 3 (2009) 569–574.
[33] M. Bruna, A.K. Ott, M. Ijas, D. Yoon, U. Sassi, A.C. Ferrari, Doping dependence of the Raman of defected graphene, ACS Nano 8 (2014) 7432–7441.
[34] W. Zhu, D. Neumayer, V. Perebeinos, P. Avouris, Silicon nitride gate dielectrics and band gap engineering in graphene layers, Nano Lett. 10 (2010) 3572–3576.
[35] Y. Zhang, T.-T. Tang, C. Girit, Z. Hao, M.C. Martin, A. Zettl, M.F. Crommie, Y.R. Shen, F. Wang, Direct observation of a widely tunable bandgap in bilayer graphene, Nature 459 (2009) 820–823.
[36] C.H. Lui, Z. Li1, K.F. Mak, E. Cappelluti, T.F. Heinz, Observation of an electrically tunable band gap in trilayer graphene, Nat. Phys. 7 (2011) 944–947.
[37] B. Huet, J.-P. Raskin, Pressure-controlled chemical vapor deposition of single-layer graphene with millimeter-size domains on thin copper film, Chem. Mater. 29 (2017) 3431–3440.
[38] B. Huet, J.-P. Raskin, Role of Cu foil in-situ annealing in controlling the size and thickness of CVD graphene domains, Carbon 129 (2018) 270–280.
[39] P. Ramnani, M.R. Neupane, S. Ge, A.A. Balandin, R.K. Lake, A. Mulchandani, Raman spectra of twisted CVD bilayer graphene, Carbon 123 (2017) 302–306.
[40] R. He, T.-F. Chung, C. Delaney, C. Keiser, L.A. Jauregui, P.M. Shand, C.C. Chancey, Y. Wang, J. Bao, Y.P. Chen, Observation of low energy Raman modes in twisted bilayer graphene, Nano Lett. 13 (2013) 3594–3601.
[41] K. Kim, S. Coh, L.Z. Tan, W. Regan, J.M. Yuk, E. Chatterjee, M.F. Crommie, M.L. Cohen, S.G. Louie, A. Zettl, Raman spectroscopy study of rotated double-layer graphene: misorientation-angle dependence of electronic structure, Phys. Rev. Lett. 108 (2012) 246103.
[42] A. Luican, G. Li, A. Reina, J. Kong, R.R. Nair, K.S. Novoselov, A.K. Geim, E.Y. Andrei, Single-layer behavior and its breakdown in twisted graphene layers, Phys. Rev. Lett. 106 (2011) 126802.
[43] S. Shallcross, S. Sharma, E. Kandelaki, O.A. Pankratov, Electronic structure of turbostratic graphene, Phys. Rev. B 81 (2010) 1.
[44] W. Liu, S. Kraemer, D. Sarkar, H. Li, P.M. Ajayan, K. Banerjee, Controllable and rapid synthesis of high-quality and large-area bernal stacked bilayer graphene using chemical vapor deposition, Chem. Mater. 26 (2014) 907–915.
[45] Q. Liu, Y. Gong, J.S. Wilt, R. Sakidja, J. Wu, Synchronous growth of AB-stacked bilayer graphene on Cu by simply controlling hydrogen pressure in CVD process, Carbon 93 (2015) 199–206.
[46] K. Yan, H. Peng, Y. Zhou, H. Li, Z. Liu, Formation of bilayer bernal graphene: layer-by-layer epitaxy via chemical vapor deposition, Nano Lett. 11 (2011) 1106–1110.
[47] W. Liu, H. Li, C. Xu, Y. Khatami, K. Banerjee, Synthesis of high-quality monolayer and bilayer graphene on copper using chemical vapor deposition, Carbon 49 (2011) 4122–4130.
[48] C. Cong, J. Jung, B. Cao, C. Qiu, X. Shen, A. Ferreira, S. Adam, T. Yu, Magnetic oscillation of optical phonon in ABA- and ABC-stacked trilayer graphene, Phys. Rev. B 91 (2015) 235403.
[49] C. Cong, T. Yu, K. Sato, J. Shang, R. Saito, G.F. Dresselhaus, M.S. Dresselhaus, Raman characterization of ABA- and ABC-stacked trilayer graphene, ACS Nano 5 (2011) 8760–8768.
[50] C.H. Lui, Z. Li, Z. Chen, P.V. Klimov, L.E. Brus, T.F. Heinz, Imaging stacking order in few-layer graphene, Nano Lett. 11 (2011) 164–169.
[51] Y. Hwangbo, C.-K. Lee, A.E. Mag-Isa, J.-W. Jang, H.-J. Lee, S.-B. Lee, S.-S. Kim, J.-H. Kim, Interlayer non-coupled optical properties for determining the number of layers in arbitrarily stacked multilayer graphenes, Carbon 77 (2014) 454–461.
[52] W. Zhu, V. Perebeinos, M. Freitag, P. Avouris, Carrier scattering, mobilities, and electrostatic potential in monolayer, bilayer, and trilayer graphene, Phys. Rev. B 80 (2009) 235402.
[53] S. Datta, Quantum Transport: Atom to Transistor, Cambridge University Press, Cambridge, England, 2005.
[54] E.H. Hwang, S. Adam, S.D. Sarma, Carrier transport in two-dimensional graphene layers, Phys. Rev. Lett. 98 (2007) 186806.
[55] M. Lazzeri, F. Mauri, Nonadiabatic Kohn anomaly in a doped graphene monolayer, Phys. Rev. Lett. 97 (2006) 266407.
[56] D.M. Basko, S. Piscanec, A.C. Ferrari, Electron-electron interactions and doping dependence of the two-phonon Raman intensity in graphene, Phys. Rev. B 80 (2009) 165413.

[57] M. Koshino, T. Ando, Orbital diamagnetism in multilayer graphenes: systematic study with the effective mass approximation, Phys. Rev. B 76 (2007) 085425.
[58] J. Yan, E.A. Henriksen, P. Kim, A. Pinczuk, Observation of anomalous phonon softening in bilayer graphene, Phys. Rev. Lett. 101 (2008) 136804.
[59] D.L. Mafra, P. Gava, L.M. Malard, R.S. Borges, G.G. Silva, J.A. Leon, F. Plentz, F. Mauri, M.A. Pimenta, Characterizing intrinsic charges in top gated bilayer graphene device by Raman spectroscopy, Carbon 50 (2012) 3435–3439.
[60] P. Gava, M. Lazzeri, A.M. Saitta, F. Mauri, Probing the electrostatic environment of bilayer graphene using Raman spectra, Phys. Rev. B 80 (2009) 155422.
[61] L.M. Malard, D.C. Elias, E.S. Alves, M.A. Pimenta, Observation of distinct electron-phonon couplings in gated bilayer graphene, Phys. Rev. Lett. 101 (2008) 257401.
[62] E.V. Castro, K.S. Novoselov, S.V. Morozov, N.M.R. Peres, J.M.B. Lopes dos Santos, J. Nilsson, F. Guinea, A.K. Geim, A.H. Castro Neto, Biased bilayer graphene: semiconductor with a gap tunable by the electric field effect, Phys. Rev. Lett. 99 (2007) 216802.